Electronic Seismologist

FastTrip: A Fast MPI-Accelerated 1D Triplication Waveform Inversion Package for Constraining Mantle Transition Zone Discontinuities

Jiaqi Li[*1], Min Chen[1,2], Keith D. Koper[3], Tong Zhou[4], Ziyi Xi[1], Shaohua Li[5], and Guoliang Li[1]

Abstract

The 410- and 660-km discontinuities define the top and bottom of the mantle transition zone (MTZ). The properties of these mineralogical phase transformation interfaces provide critical constraints on the dynamics, temperature, and composition of the MTZ. Triplicated body waves that bottom near these discontinuities carry rich information about them. To streamline the modeling of upper-mantle triplications recorded at regional distances (13°–30°), we have developed a (Fast) Message Passing Interface (MPI)-accelerated 1D (Tr)iplication Waveform (I)nversion (P)ackage (FastTrip). With triplication waveform data as input, FastTrip uses a global search method to output a set of acceptable 1D velocity models. Quantitative estimation of the model uncertainties can be further derived based on the range of acceptable models. FastTrip supports central processing unit (CPU) parallel acceleration (15,000 models within 2 hr with 100 CPUs) and is portable to other inversion problems that can be described by a relatively small number of model parameters.

Cite this article as Li, J., M. Chen, K. D. Koper, T. Zhou, Z. Xi, S. Li, and G. Li (2021). FastTrip: A Fast MPI-Accelerated 1D Triplication Waveform Inversion Package for Constraining Mantle Transition Zone Discontinuities, *Seismol. Res. Lett.* **92**, 2647–2656, doi: 10.1785/0220200475.

Supplemental Material

Introduction

The 410- and 660-km discontinuities define the top and bottom of the mantle transition zone (MTZ). The 410-km discontinuity represents the mineralogical phase change from olivine to wadsleyite, and the 660-km discontinuity marks the dissociation of ringwoodite to bridgmanite and Magnesiowustite (e.g., Ringwood, 1975; Ito and Takahashi, 1989). Knowledge of the seismic structures of these discontinuities provides critical constraints on several significant scientific questions, including the pattern of the mantle convection (e.g., Morgan and Shearer, 1993), deep water cycles of the Earth (e.g., Helffrich and Wood, 1996; Bercovici and Karato, 2003; Kawakatsu and Watada, 2007), the Earth's internal temperature field (e.g., Vidale and Benz, 1992), and mechanisms for deep-focus earthquakes (e.g., Green and Burnley, 1989; Kirby *et al.*, 1991).

MTZ discontinuities can be detected and studied using secondary seismic phases generated at the interface (e.g., Flanagan and Shearer, 1998, 1999; Gu and Dziewonski, 2002; Niu *et al.*, 2005; Ritsema *et al.*, 2009; Wang *et al.*, 2017; Li *et al.*, 2019; Tian *et al.*, 2020). However, stacking techniques (over hundreds of traces) are typically needed to enhance visibility (Shearer, 2000). Body-wave triplications that bottom near the MTZ discontinuities can also effectively constrain these interfaces (Wang *et al.*, 2009). Moreover, unlike the minor phases, triplications can be clearly recorded by a single station without stacking.

The travel times of triplications have been used to constrain major mantle discontinuities since 1965 (e.g., Niazi and Anderson, 1965; Johnson, 1967). Besides, waveform information has also been used, through synthetic waveform modeling, to constrain the best-fitting 1D velocity–depth profile (e.g., Grand and Helmberger, 1984; Tajima and Grand, 1995; Brudzinski and Chen, 2000). However, because of the complexity of the triplicated waveforms, most results are obtained by the trial-and-error approach. To automate the inversion process, Gao *et al.* (2006) have applied the conjugate gradient method into the triplication inversion, although choosing the

1. Department of Computational Mathematics, Science and Engineering, Michigan State University, East Lansing, Michigan, U.S.A., https://orcid.org/0000-0001-7525-5401 (JL); http://orcid.org/0000-0002-6970-7317 (MC); https://orcid.org/0000-0001-8601-8946 (GL); 2. Department of Earth and Environmental Sciences, Michigan State University, East Lansing, Michigan, U.S.A.; 3. Department of Geology and Geophysics, University of Utah, Salt Lake City, Utah, U.S.A., https://orcid.org/0000-0002-9725-6509 (KDK); 4. Earth, Planetary and Space Sciences, University of California Los Angeles, Los Angeles, California, U.S.A.; 5. Lanzhou Institute of Geotechnique and Earthquake, China Earthquake Administration, Lanzhou, Gansu, China, https://orcid.org/0000-0003-2882-7723 (SL)

*Corresponding author: lijiaqi9@msu.edu

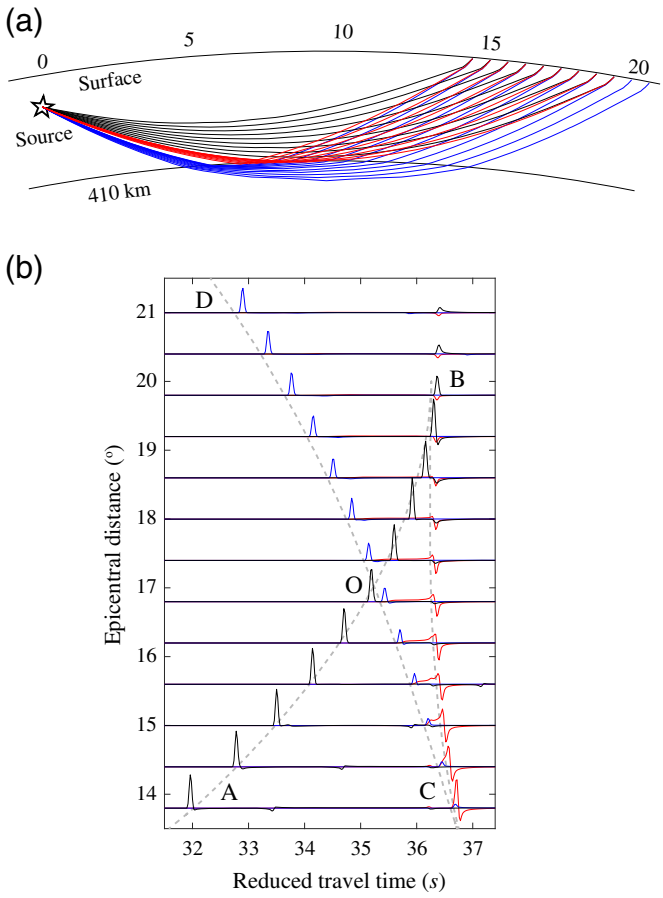

Figure 1. Ray paths and corresponding waveforms for triplications. (a) Ray paths for the triplicated *P* waves. The black star is the earthquake source at 114 km. Black, red, and blue lines are the ray paths for the direct waves (AB), reflected waves (BC), and refracted waves (CD), respectively. Their corresponding displacement waveforms are shown in (b) with the same color. Dashed gray lines in (b) are the travel-time curves calculated by Taup (Crotwell *et al.*, 1999). A reducing slowness of 11.5 s/° is used for the time plot. The color version of this figure is available only in the electronic edition.

initial model and avoiding the local minima can be challenging for such gradient-based inversion. The grid-search method has also been used to model triplicated waveforms. Considering the huge computational cost of such exhaustive grid search, a prestep of trial-and-error forward modeling is often needed (e.g., Chu *et al.*, 2012), and the grid-search part can only deal with a reduced number of model parameters (e.g., Chu *et al.*, 2012; Li *et al.*, 2017). Moreover, estimation for the model uncertainties and possible trade-off between parameters is hard to derive quantitatively (Shearer, 2000).

Recently, the 3D full waveform inversion has also incorporated triplication waveforms into its database (Tao *et al.*, 2018). However, the current 3D inversion at the relatively low-frequency band (8 s or longer) cannot take the full information of the triplicated phases, which are only several seconds apart. Besides, the available data may still not be adequate to constrain a 3D model well. Therefore, 1D simulation and inversion with much higher frequency (up to ~1 Hz) and fewer parameters are still powerful tools to reveal the seismic structure in certain regions, especially near the turning points of ray paths.

In this article, we introduce our (Fast) MPI-accelerated 1D (Tr)iplication Waveform (I)nversion (P)ackage (FastTrip). Based on a niching genetic algorithm (NGA), FastTrip can search for maximally diverse sets of 1D velocity–depth profiles that fit the triplication data. This method is more likely to find the global minimum regardless of the initial model and is faster than using an exhaustive grid search. Moreover, a series of acceptable models are helpful to evaluate the model uncertainties. Finally, we will show the efficiency of the central processing unit (CPU)-parallelization accelerated version of FastTrip.

Method

When velocity increases sharply with depth (either steep gradients or discontinuities), body waves will propagate in different paths. Here, we take the 410-km discontinuity in the IASP91 model (Kennett and Engdahl, 1991), with an intermediate-depth earthquake from the Global Centroid Moment Tensor catalog (Dziewonski and Woodhouse, 1983) as an example. The focal depth is 114 km (Fig. 1a), and only *P* waves are shown (Fig. 1b). Within a specific epicentral distance range, these multipathing body waves (AB, waves turning above the discontinuity; BC, waves reflected by the discontinuity; CD, waves transmitted through the discontinuity) provide dense subhorizontal ray coverage in the vicinity of the discontinuity (Fig. 1a,b).

In this section, we use simple synthetic seismograms (delta source time function and no attenuation) generated by the WKBJ code (Chapman, 1978) to display each branch of the multipathing phases explicitly (Fig. 1b). Other waveforms in the Synthetic Test and Discussion sections of this article are convolved with a Gaussian function (~2 s) and a t^*(~1 s) to represent the source time function and *P*-wave attenuation, respectively.

As a full waveform inversion problem, the basic procedure consists of three parts. First, we perform forward modeling to generate synthetic waveforms based on a given 1D velocity model. Next, we compare the synthetics and the recorded waveforms with a particular misfit function. Finally, we update the model to decrease the misfit. In this way, these three steps continue to iterate until convergence.

The most challenging part lies in the model updating part. To obtain quantitative error bounds and avoid the risk of falling into the local minima faced by the gradient-based inversion method, we adopt an NGA (Koper *et al.*, 1999; Li *et al.*, 2012) into the inversion framework of triplicated waveforms. NGAs are non-gradient-based inversion schemes that search the

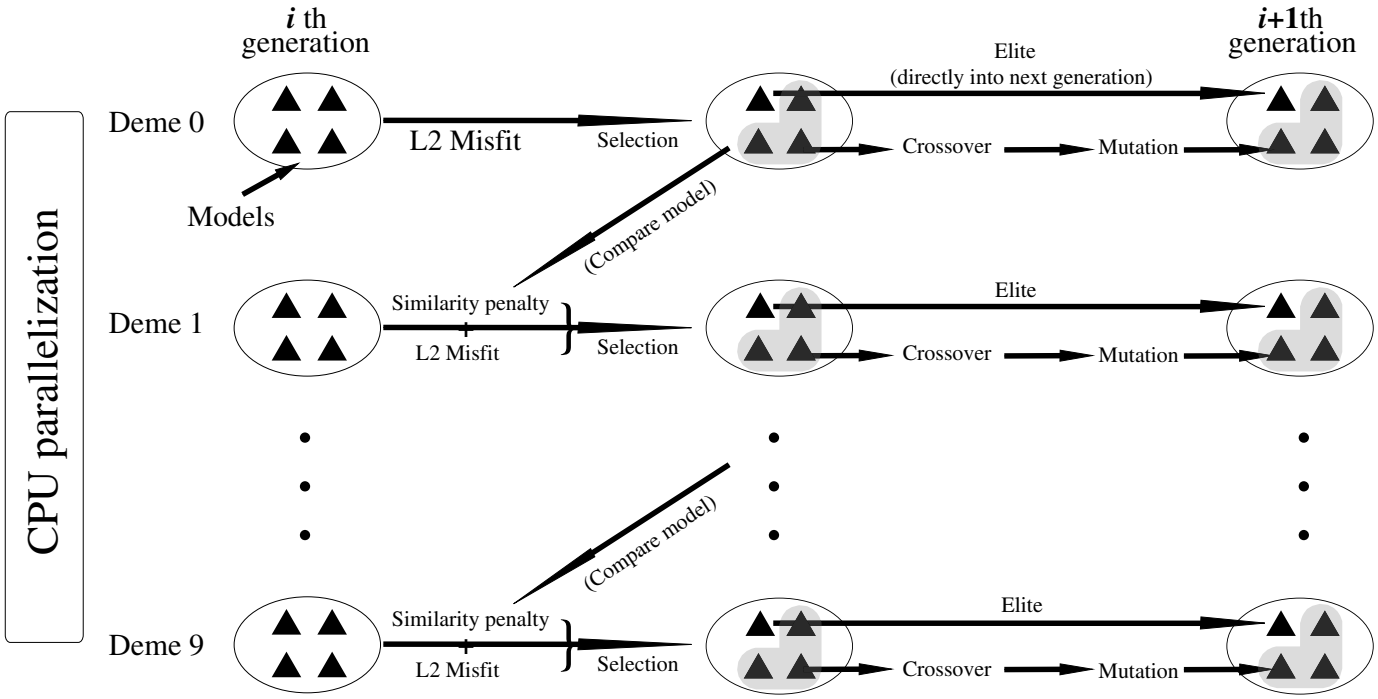

Figure 2. The concept for the MPI-accelerated niching genetic algorithm. Black triangles represent models. In the *i*th generation, these models are equally divided into 10 demes. In deme 0, these models are directly selected based on the L2-norm misfit between data and synthetics. The best model (elite) can directly go into the next generation, whereas other models need further crossover and mutation. In other demes, besides the L2-norm misfit used in deme 0, an additional similarity penalty term is applied to ensure model diversity among different demes. In each generation, all the models in the 10 demes are independent and can be simultaneously calculated through central processing unit (CPU) parallelization.

model space through massive forward modeling, however, in general, much faster than the exhaustive grid-search techniques. NGAs inherit three advantages from the traditional genetic algorithm: First, NGAs are independent of the initial model. Only the search range of the model space is a priori. Within this range, NGAs will randomly generate a large number of models as initial models. And then, models will be updated through "crossover" and "selection." Second, NGAs allow "mutation" for model parameters, which means they have a probability of 1%–5% to change their values in each iteration to avoid falling into the local minimums. Third, because NGAs involve numerous samplings in the model space, they can finally output a series of acceptable model sets. The mean and variance of these acceptable models can help estimate the uncertainty of the final model.

The key difference between NGAs and other global search techniques, such as Monte Carlo Markov chain (e.g., Mosegaard and Tarantola, 1995), genetic algorithms (e.g., Stoffa and Sen, 1991), simulated annealing (e.g., Bina, 1998), is that NGAs promote model diversity while simultaneously identifying models with low misfits. Selection for diversity is accomplished by dividing the model population into subpopulations or "demes." The models in each "deme" may be similar to one another, but models in different "demes" are not alike (Fig. 2). Specifically, a penalty term for the model similarities between "demes" is applied to ensure the model diversity (Koper *et al.*, 1999). In this way, different species of solutions can evolve to exploit different regions of model space (niches) that have low misfit. Therefore, NGAs are suitable for handling geophysical inversion problems with multiple local minima.

Implementation

Prerequisite

Operation system: Linux.

Essential software: MPICH, and a FORTRAN compiler.

Python modules: NumPy, SciPy, and Mpi4Py.

The tutorial for the environment setup is included in the FastTrip package (see Data and Resources). After these preparations, we can use FastTrip to obtain 1D velocity–depth profiles with waveforms from an earthquake, recorded by a seismic network (Fig. 3). In this section, we will introduce the folder structure and necessary parameters.

Preparing waveform data and inversion window

The waveform data to use could either be the ground displacement data or the ground velocity data. Therefore, instrument response should be removed by the user. Other related routine operations, such as demean, detrend, tapering, and filtering, should also be applied before the inversion. For the synthetic

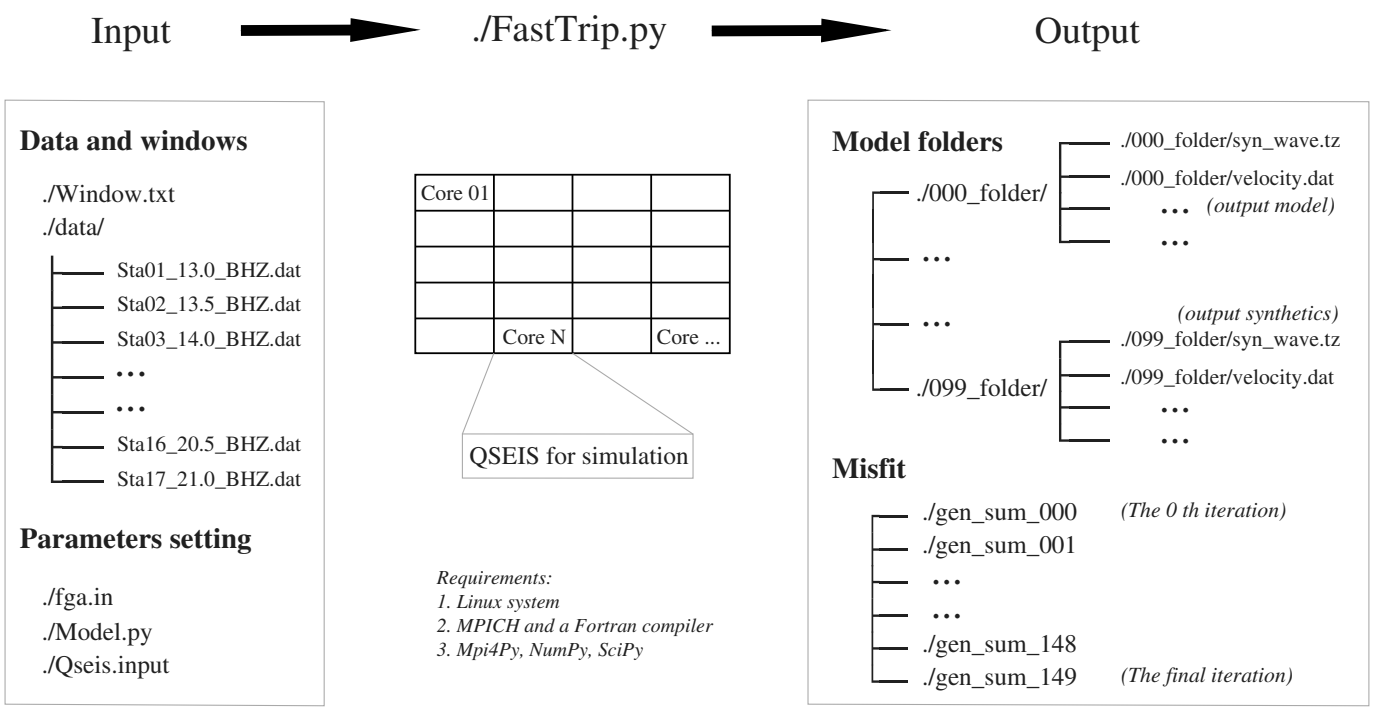

Figure 3. The schematic diagram for the usage of the (Fast) MPI-accelerated 1D (Tr)iplication Waveform (I)nversion (P)ackage (FastTrip). Input files consist of the recorded waveforms (in the "./data/" folder), misfit windows ("./Window.txt"), station and earthquake information ("./Qseis.input"), model information ("./Model.py"), and searching range for the model parameters ("./fga.in"). FastTrip will search the model space through massive modeling. This process can be accelerated through CPU parallelization (1–100 cores). Output files contain the misfit and model information throughout the entire inversion (e.g., "./gen_sum_149" is for the 149th generation) and the synthetic waveforms for all the 100 models in the last generation (e.g., "./000_folder/syn_wave.tz" is for the first model).

case in this article, the earthquake is recorded by a linear seismic network comprising 17 stations.

Compared with the total trace length of 100 s, the triplication wavetrain duration is less than 20 s. To avoid interferences from noise and other signals, we need to specify an inversion window, only within which the misfit for the waveform is considered. This inversion window is specified in the file "./Window.txt" (Fig. 4c).

Alignment of the data and synthetics is widely used in triplication studies (e.g., Grand and Helmberger, 1984; LeFevre and Helmberger, 1989; Brudzinski and Chen, 2003; Wang and Niu, 2010; Chu *et al.*, 2012; Zhang *et al.*, 2012), because it can mitigate baseline errors associated with uncertainties in earthquake origin time and shallow Earth structure, and emphasize the relative time and amplitude between the triplicated phases. In FastTrip, we adopt cross correlation to implement the alignment. Accordingly, the first controlling line in Figure 4c denotes this cross-correlation window (dashed box in Fig. 4a). We note that this window is only for alignment, and no misfit is calculated in this alignment window.

The second and third lines control the misfit windows (Fig. 4c). We specifically set two windows (win 1 and win 2) for each station, because usually there is more than one phase, as shown in Figure 4a. Furthermore, there is also noise between these two phases. Therefore, we want to replace one long continuous window with two short windows. Furthermore, with two windows, we can give different weights to different triplicated phases. In some simple cases, if one window is adequate, we could either set the second window the same as the first one or set the second window weight to zero.

Setting up the model parameters

As this is a non-gradient-based inversion, we only need to specify search ranges for the model parameters. Within this range, FastTrip will generate initial models as well as update new models. Specifically, the model structure is set as a depth–velocity profile in the "./Model.py" file (Fig. 5a). Model parameters (V_P, V_S, and density) are given at each anchor point of depth. They can be either fixed values or parameters to invert for. If this parameter is set to be inverted for, its corresponding variation range is set in the "./fga.in" file (Fig. 5b). In this case, two of them are immediately on the discontinuity to capture the velocity jump. Other anchor points away from the interface, with an interval of ~40 km, represent gradual features. Between these anchor points, the velocity is linearly interpolated.

As shown in Figure 5c, the *P*-wave velocity at each anchor point is allowed to vary within ±0.3 km/s, and the position of

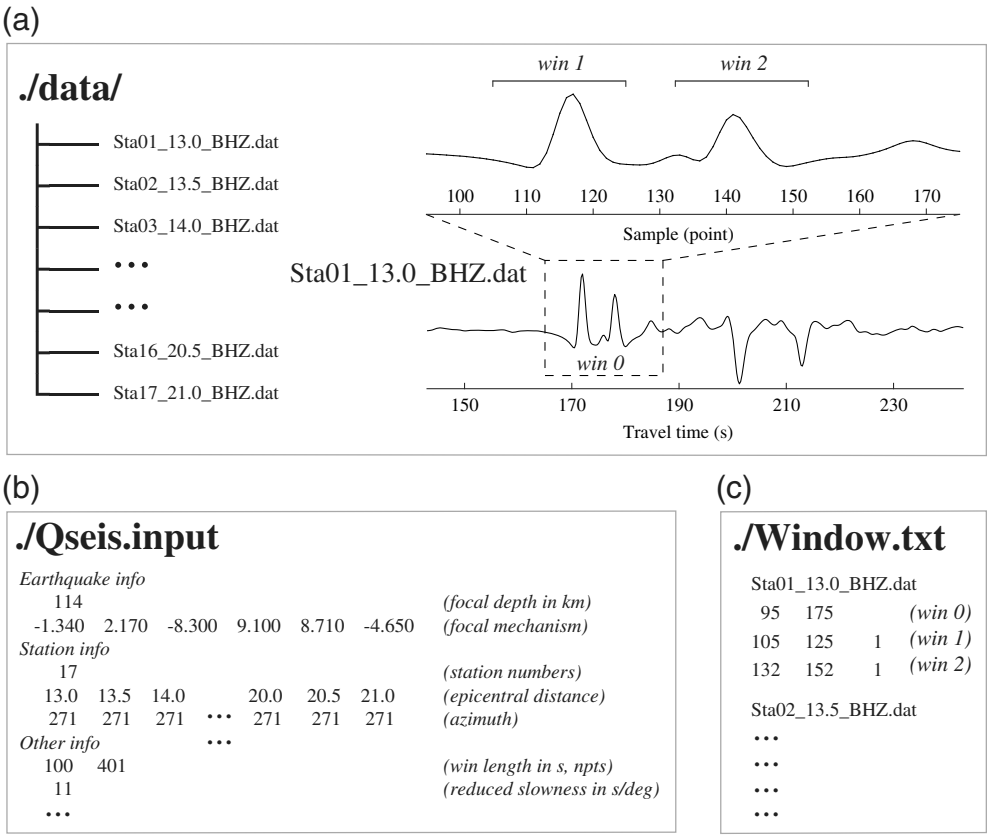

Figure 4. Examples for the input files. (a) The left side is the structure of the "./data/" folder. The lower right waveform is for one of the files ("/.data/Sta01_13.0_BHZ.dat"), with the *x* axis as the travel time. The upper right side shows the zoomed-in waveform in the alignment window, with the *x* axis as the sampling point. Above the waveform, two misfit windows are shown. (b) Some essential parameters in the "./Qseis.input" file. (c) Inversion window file. The first line indicates the station name. The following three lines are the alignment window and two misfit windows shown in (a). The third column indicates the weightings for the misfit windows.

Calculating waveform misfit

Waveform misfit is calculated within the misfit windows after cross-correlation alignment. As such, we first cross-correlate the observed and theoretical waveform for each station (e.g., the *i*th) to obtain the travel time difference Δt_i. Then, we calculate the L2 norm of the differences between the observed waveform and aligned synthetic one as the misfit function χ_{L2}:

$$\chi_{L2} = \sum_{i=1}^{N} \int_{t_1}^{t_2} |\mathbf{d}(\mathbf{x}_i, t) - \mathbf{u}(\mathbf{x}_i, t + \Delta t_i)|^2 dt, \quad (1)$$

in which $\mathbf{d}(\mathbf{x}_i, t)$ is the observed waveform recorded by the *i*th station, $\mathbf{u}(\mathbf{x}_i, t + \Delta t_i)$ is the synthetic waveform for the *i*th station after a Δt_i time shift. The start point and end point for the misfit window are represented by t_1 and t_2, respectively. N marks the total station number used in the inversion.

In this example, we choose the L2 norm of waveform differences in the time domain as the misfit function. Alternatively, we can also specify our desired form of the misfit function in the "./FastTrip.py" file.

the discontinuity also varies within ±20 km, based on the IASP91 model. With these settings, FastTrip will generate 100 (10 demes × 10 models/deme) model folders (Fig. 6a). In each model folder (e.g., "./000_folder"), the model parameter file is stored in a more readable velocity–depth format in the "./000_folder/velocity.dat" file (Fig. 6c). As the inversion progresses, these velocity files in the model folders will also be updated accordingly.

Simulating synthetic seismograms

As a global search type of inversion scheme, FastTrip requires numerous simulations in the model space. To reduce the vast amount of computation time for the forward modeling, we choose an orthonormal propagator algorithm QSEIS (Wang, 1999) for simulation. For a given source, QSEIS can directly calculate waveforms starting from the onset time of the triplication phases instead of the origin time of the earthquake, which significantly saves computing resources. This technique is implemented by applying a "reduced slowness" in the "./Qseis.input" file (Fig. 4b).

Output files

The first output file is the corresponding waveform file stored in each model folder. We take the first model folder as an example, where the original vertical synthetic waveforms calculated by QSEIS (without attenuation) are stored in "./000_folder/syn_seis.tz." Based on these original synthetics, two more stages are applied in the "./FastTrip.py" script. We first filter the original synthetics using the same frequency band we applied to the observed data to make them comparable. Then, we convolve a constant t^* value of 1 s to represent attenuation for the *P* wave. After these, the final output is stored in "./000_folder/syn_wave.tz" (Fig. 6b).

The other output files are the inverted models and the waveform misfits during the iterations. We take the final iteration (the 149th) as an example, as shown in the "./gen_sum_149"

(a)

./Model.py

```
...
CoreNumbers    =  10;
...
depth[0]   =   0;          vp[0]    =  5.80;
depth[1]   =  20;          vp[1]    =  5.80;
depth[2]   =  20;          vp[2]    =  6.50;
depth[3]   =  35;          vp[3]    =  6.50;
depth[4]   =  35;          vp[4]    =  8.04;
depth[5]   = 120;          vp[5]    =  8.05;
depth[6]   = 165;          vp[6]    =  8.18;
depth[7]   = 210;          vp[7]    =  8.30;
depth[8]   = 250;          vp[8]    =  8.45+par[0];
depth[9]   = 290;          vp[9]    =  8.60+par[1];
depth[10]  = 330;          vp[10]   =  8.74+par[2];
depth[11]  = 370;          vp[11]   =  8.88+par[3];
depth[12]  = 410+par[9];   vp[12]   =  9.03+par[4];
depth[13]  = 410+par[9];   vp[13]   =  9.36+par[5];
depth[14]  = 450;          vp[14]   =  9.50+par[6];
depth[15]  = 490;          vp[15]   =  9.63+par[7];
depth[16]  = 530;          vp[16]   =  9.76+par[8];
depth[17]  = 570;          vp[17]   =  9.90;
depth[18]  = 600;          vp[18]   = 10.00;
depth[19]  = 660;          vp[19]   = 10.20;
...
...
```

(b)

./fga.in

```
...
-0.3   0.3     (par[0])
-0.3   0.3     (par[1])
...
-0.3   0.3     (par[7])
-0.3   0.3     (par[8])
 -20    20     (par[9])
```

(c)

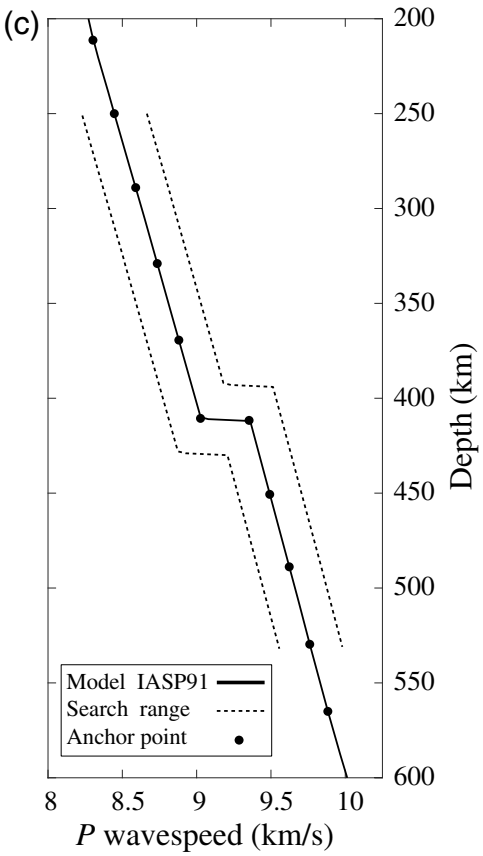

Figure 5. Examples for the model setup. (a) The velocity–depth profile is stored in two NumPy arrays (depth[] and vp[]). When there is a "par[]," it means this parameter is to invert; otherwise, it is a fixed value. "CoreNumbers" indicates the number of cores used. (b) Searching ranges for the parameters. (c) The solid black line is the IASP91 model. Black dots are the anchor points shown in (a). Dashed black lines mark the searching range. In this case, the velocity varies within ±0.3 km/s, and the interface depth varies within ±20 km, as shown in (b).

file (Fig. 6d). There are 10 demes (00 to 09). In each deme, the first column represents the model name (000 to 009), and the second column denotes the relative misfit. Within certain deme, a smaller misfit indicates a better model.

Synthetic test

To verify the correctness and stability of FastTrip, we designed a *P*-wave synthetic test. In this test, we choose the IASP91 model as the ground-truth model. First, we generate its corresponding displacement waveforms. Then, we use these synthetics from IASP91 as the input for FastTrip.

In the model setup, considering the penetration depth ranges of the ray paths, we only invert for the structure between 210 and 570 km. Beyond this depth range, the model is fixed to the IASP91 model. To simplify the problem in this test, the *P*-wave velocity is the only unknown parameter for each anchor point, whereas the density and the Poisson's ratio are the same as the values in the IASP91 model. In this case, there are in total 10 parameters to invert for: nine velocity anchor points and an additional parameter represents the depth variation of the discontinuity (Fig. 5a).

In this ideal case, without noise, we use a continuous misfit window for each trace. This inversion window starts from 32 s and ends at 52 s (reduced time), which contains the entire triplicated *P* wavetrain. The model comparison results show that the accepted model sets (the shaded yellow region in Fig. 7a) converge to the ground-truth model. We further use the best model (red line) to generate the corresponding inverted waveforms to examine the waveform fitting. The differences between the ground-truth waveforms and the inverted waveforms are minimal (Fig. 7b). Moreover, the residual evolution shows that this method converges very quickly (Fig. 7c). Specifically, after 20 generations (100 simulations in each generation), the residuals significantly reduce, and after 60 generations, the residuals converge.

Discussion

Uncertainty estimation

After 15,000 model evaluations, besides the best model (in red color), we have also discovered a set of acceptable models (the shaded yellow region in Fig. 7a). Here, we determine the misfit threshold for the acceptable models by visually comparing the synthetics and data. In this case without noise, a misfit increase of 30% than the best model can cause an obvious mismatch in the waveform and is set to be the upper limit. The best model (in red color) is very close to the input IASP91 model. Another model (in blue color) shows a 10 km uplift of the discontinuity and a low-velocity zone above it. The waveforms between these two models are almost identical, and

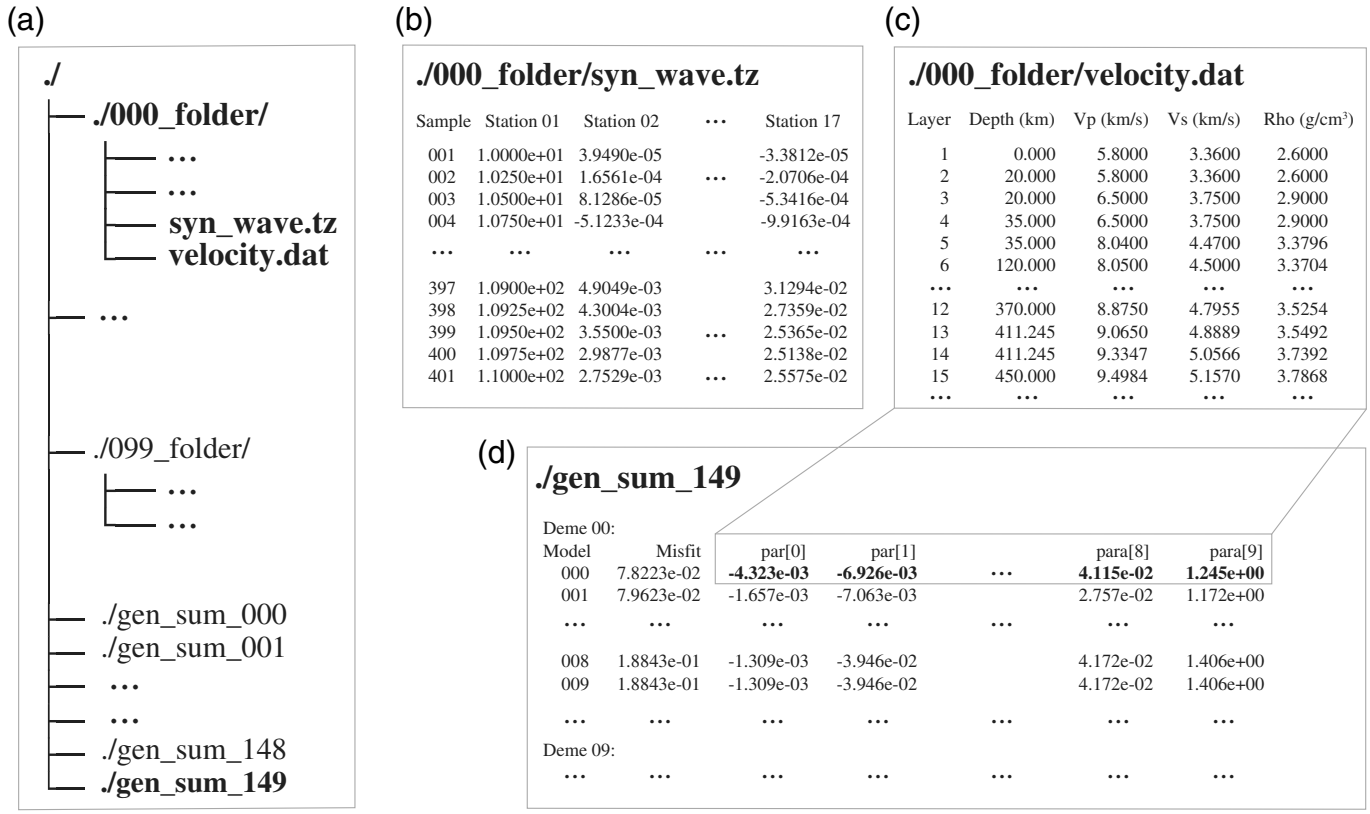

Figure 6. Examples for the output files. (a) The structure for all the output files. (b) Example for the synthetic waveforms, where there are 17 stations for this case. (c) The inverted velocity–depth profile for the first model in the 149th generation. (d) The misfit and model information for the 149th generation. The first column is the model name in each deme, the second column shows the relative misfit, and the following columns are the inverted model parameters (similar to (c)).

both of them are also quite similar to the IASP91 model's waveforms (Fig. 7b).

These results reflect the trade-off between the discontinuity depth and the velocity above it. Specifically, for this second model, the 10 km uplifted interface is equivalent to a localized high-velocity anomaly between 400 and 410 km. On the contrary, a low-velocity zone above the interface can, to some extent, cancel out the high-velocity anomaly effect. This synthetic test shows that FastTrip can effectively obtain diverse high-quality models. Moreover, FastTrip could help analyze the possible trade-offs between model parameters and further estimate model uncertainty.

Robustness of the inversion

For intuitive analysis of the triplication waveforms, in the synthetic test earlier, we assume an ideal case in which there are neither noises in the data nor errors in the source and model parameters. However, in the real case, uncertain source parameters, unknown shallow structures, and random seismic noises will cause difficulties to triplication inversion. Therefore, we further conduct a series of more realistic tests to verify the robustness of FastTrip.

Uncertainty in source parameters. Here, we focus on the uncertainty in the focal depth instead of the horizontal location, because focal depth is usually less constrained in most earthquake bulletins and catalogs. We first explore the waveform's sensitivity to the focal depth through the forward modeling. The reference focal depth is 114 km. Given a source half-duration of 2.0 s, focal depth variations within ±10 km will not cause obvious changes to the relative time and amplitudes between triplicated phases (Fig. S1a, available in the supplemental material to this article), due to the finite-frequency effect. We further set two more extreme situations in which the focal depths are set −25 and +25 km deviated from the reference focal depth and then perform the waveform inversion with these inaccurate depth values. Results show that models with good waveform fitting (Fig. S1b) show deviated interface depths by about −14 and +13 km, respectively (Fig. S1c). We note that the difference between the error in the focal depth (∼25 km) and the inverted depth deviation of the interface (∼14 km) is comparable to the resolution limit of ∼10 km (Fig. S1a).

To conclude, small uncertainty (approximately one wavelength) of the focal depth will not influence the inversion

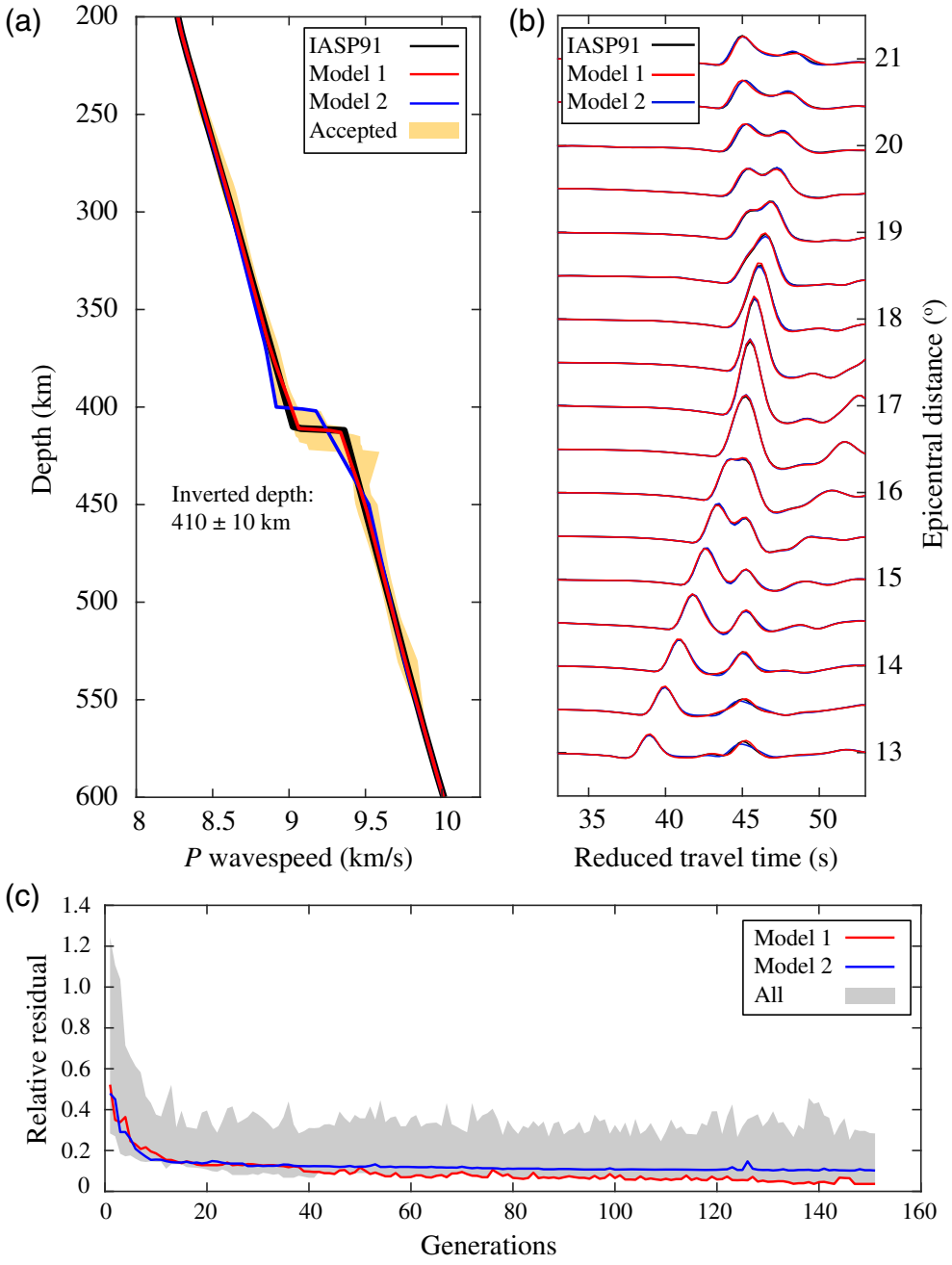

Figure 7. *P*-wave synthetic tests for FastTrip. (a) Inverted models. The solid black line is the ground-truth IASP91 model. The dashed yellow region indicates the "intersection" of all the acceptable models. The red line is the best-fitting model, and the blue line is another acceptable model. (b) Waveform fitting. The black waveforms are synthetic data for the IASP91 model. Red and blue waveforms are synthetics for the models with the same color in (a). (c) Residual between data and synthetics with respect to generations. The shaded gray region shows the misfits for all the models. Red and blue lines are the residual for the models with the same color in (a). The color version of this figure is available only in the electronic edition.

results much. However, extreme error in the focal depth will cause a corresponding deviation to the inverted model. Nevertheless, for most of the triplication studies, the focal depth is often reconstrained from the depth phases to ensure its accuracy.

We have also tested the influence of the uncertainty in the source time function (ground-truth half-duration is 2.0 s) by setting the half-durations used in the inversion to be 1.0, 1.5, 2.5, and 3.0 s, respectively. Results show that the inaccurate source half-duration will not affect much finding the best model, although the overall waveform fittings are not as good (Fig. S2).

Uncertainty in shallow structures. In the synthetic test earlier, we only invert for the structure deeper than the penetration depth (~200 km) of the seismic ray for the nearest station. For the shallower structure (e.g., crust or uppermost mantle), where triplications do not have enough ray coverage, the ideal case is that the structure is preconstrained by other approaches (e.g., Chu and Helmberger, 2014). However, for earthquakes in subduction zones, there are not enough nearby stations to refine the shallow part. Nevertheless, triplications are less sensitive to very shallow structures owing to the similar ray paths away from the turning points. For the quantitative investigation, we have designed a corresponding synthetic case in which the *P*-wave velocity in the uppermost 50 km deviates from the ground-truth model by −5% (to represent a more generalized situation, we set a 2D anomaly in this test as shown in Fig. S3a). Although the absolute travel times will be delayed, the relative times and amplitudes will not be much influenced (Fig. S3b). Therefore, with the implementation of alignment in FastTrip, the ground-truth model can still be recovered in the deeper part (Fig. S3c).

Noise in the data. We have added both the random Gaussian noises (Fig. S4a,b) and real noises (Fig. S4c) to the synthetic data. In all these three cases with noises added in, the first-order pattern of triplication waveforms is fitted, and the best model inverted is close to the ground-truth model (Fig. S4d).

Speed up by CPU parallelization

Each forward calculation, with a source half-duration of 2.0 s, can be completed within 20 s. However, given the total number of 15,000 models (10 demes × 10 models × 150 generations) in our example, more than ∼80 hr are needed. Calculations between iterations can only be performed serially, because models in the $i+1$th generation depend on models from the previous ith generation. Nevertheless, within each generation, the 100 models are independent of each other. Therefore, we can use a parallelization strategy to simultaneously evaluate all the models in each generation.

The number of available CPUs is specified by changing the "CoreNumbers" in the "./Model.py" file (Fig. 5a). For example, with a personal computer, we could set "CoreNumbers" to four to eight, and with a work station or cluster, we could set it to a higher value. In this case, we set the "CoreNumbers" to 100, where we can achieve the maximum acceleration in each iteration. Under this setting, the total inversion with 15,000 model samplings is done within 2 hr.

Portability to other inversion problems

By modularization and separation of the processes of model construction, forward modeling, misfit measurement, and model optimization, FastTrip provides a framework that can be generalized to other inversion problems. Furthermore, because the CPU-parallelization is set in "Model.py," which is independent of the forward modeling tool, it enhances the portability of FastTrip. For the current implementation of FastTrip, we choose QSEIS to perform the forward simulation. Alternatively, we can also switch to other modeling software, with little modification to ensure the format of the input and output files. Possible alternative software includes a similar frequency–wavenumber program (Zhu and Rivera, 2002) and the classic WKBJ program (Chapman, 1978). In the future, more choices of the forward modeling and model optimization tools will be included in a modular form to promote portability.

In addition to its compatibility with different simulation tools, FastTrip is not limited to this specific triplication inversion. As long as we measure the differences between the data and the synthetics and update the 1D model based on the misfit, FastTrip is portable. Therefore, several geophysical studies, such as the receiver function, *SS* precursors, and focal mechanism inversion, are suitable because of the generalized framework of FastTrip.

Conclusion

Multipathing, that is, triplicated, body waves bottom near the discontinuity and carry rich information, such as interface depth and velocity jump across it. The non-gradient-based inversion package FastTrip automates the triplication inversion process and outputs a set of acceptable 1D depth profiles of the velocity. FastTrip can also be used as a tool to explore model uncertainties. Furthermore, FastTrip is very efficient under CPU parallel acceleration, with essentially linear speed-up, and is portable to other inversion problems.

Data and Resources

Detailed synthetic settings and results for the Robustness of the Inversion section are included in the supplemental material. The (Fast) MPI-accelerated 1D (Tr)iplication Waveform (I)nversion (P)ackage (FastTrip), user manual, and example files are available on Github at https://github.com/lijiaqi0315/FastTrip (last accessed March 2021). The authors are glad to share the digital data, data processing scripts, plotting scripts for the readers to reproduce the figures in this article. You are welcome to contact the author (lijiaqi9@msu.edu) for detailed guidance on using FastTrip or its application to your own work.

Declaration of Competing Interests

The authors acknowledge that there are no conflicts of interest recorded.

Acknowledgments

The authors thank Tiezhao Bao, Yanbin Wang (Peking University), Zhigang Peng (Georgia Tech), Editor-in-Chief Allison Bent, Managing Editor Annastasia Pratt, and two anonymous reviewers for their valuable advice and help. The authors appreciate Rongjiang Wang (GFZ) for providing the source code of QSEIS. They thank the Institute for Cyber-Enabled Research (ICER) at Michigan State University, the Extreme Science and Engineering Discovery Environment (XSEDE supported by National Science Foundation [NSF] Grant ACI-1053575), and the High-performance Computing Platform of Peking University for providing the high-performance computing resources. The authors thank the Incorporated Research Institutions for Seismology (IRIS) Data Management Center for the access to waveforms (noise record) used in Figure S4c. This research was supported by NSF Grant 1802247 and the startup fund of Min Chen at Michigan State University.

References

Bercovici, D., and S.-I. Karato (2003). Whole-mantle convection and the transition-zone water filter, *Nature* **425,** no. 6953, 39–44.

Bina, C. R. (1998). Free energy minimization by simulated annealing with applications to lithospheric slabs and mantle plumes, in *Geodynamics of Lithosphere and Earth's Mantle*, Springer, 605–618.

Brudzinski, M. R., and W.-P. Chen (2000). Variations in *P* wave speeds and outboard earthquakes: Evidence for a petrologic anomaly in the mantle transition zone, *J. Geophys. Res.* **105,** no. B9, 21,661–21,682.

Brudzinski, M. R., and W.-P. Chen (2003). A petrologic anomaly accompanying outboard earthquakes beneath Fiji-Tonga: Corresponding evidence from broadband *P* and *S* waveforms, *J. Geophys. Res.* **108,** no. B6, doi: 10.1029/2002JB002012.

Chapman, C. H. (1978). A new method for computing synthetic seismograms, *Geophys. J. Int.* **54,** no. 3, 481–518.

Chu, R., and D. Helmberger (2014). Lithospheric waveguide beneath the midwestern United States; massive low-velocity zone in the lower crust, *Geochem. Geophys. Geosys.* **15,** no. 4, 1348–1362.

Chu, R., B. Schmandt, and D. V. Helmberger (2012). Upper mantle *P* velocity structure beneath the midwestern United States derived from triplicated waveforms, *Geochem. Geophys. Geosys.* **13,** no. 2, doi: 10.1029/2011GC003818.

Crotwell, H. P., T. J. Owens, and J. Ritsema (1999). The TauP Toolkit: Flexible seismic travel-time and ray-path utilities, *Seismol. Res. Lett.* **70,** no. 2, 154–160.

Dziewonski, A. M., and J. H. Woodhouse (1983). An experiment in systematic study of global seismicity: Centroid-moment tensor solutions for 201 moderate and large earthquakes of 1981, *J. Geophys. Res.* **88,** no. B4, 3247–3271.

Flanagan, M. P., and P. M. Shearer (1998). Global mapping of topography on transition zone velocity discontinuities by stacking *SS* precursors, *J. Geophys. Res.* **103,** no. B2, 2673–2692.

Flanagan, M. P., and P. M. Shearer (1999). A map of topography on the 410-km discontinuity from *PP* precursors, *Geophys. Res. Lett.* **26,** no. 5, 549–552.

Gao, W., E. Matzel, and S. P. Grand (2006). Upper mantle seismic structure beneath eastern Mexico determined from *P* and *S* waveform inversion and its implications, *J. Geophys. Res.* **111,** no. B8, doi: 10.1029/2006JB004304.

Grand, S. P., and D. V. Helmberger (1984). Upper mantle shear structure of North America, *Geophys. J. Int.* **76,** no. 2, 399–438.

Green, H., II, and P. Burnley (1989). A new self-organizing mechanism for deep-focus earthquakes, *Nature* **341,** no. 6244, 733–737.

Gu, Y. J., and A. M. Dziewonski (2002). Global variability of transition zone thickness, *J. Geophys. Res.* **107,** no. B7, ESE–2.

Helffrich, G. R., and B. J. Wood (1996). 410 km discontinuity sharpness and the form of the olivine $\alpha - \beta$ phase diagram: Resolution of apparent seismic contradictions, *Geophys. J. Int.* **126,** no. 2, F7–F12.

Ito, E., and E. Takahashi (1989). Postspinel transformations in the system Mg_2SiO_4-Fe_2SiO_4 and some geophysical implications, *J. Geophys. Res.* **94,** no. B8, 10,637–10,646.

Johnson, L. R. (1967). Array measurements of *P* velocities in the upper mantle, *J. Geophys. Res.* **72,** no. 24, 6309–6325.

Kawakatsu, H., and S. Watada (2007). Seismic evidence for deep-water transportation in the mantle, *Science* **316,** no. 5830, 1468–1471.

Kennett, B., and E. Engdahl (1991). Traveltimes for global earthquake location and phase identification, *Geophys. J. Int.* **105,** no. 2, 429–465.

Kirby, S. H., W. B. Durham, and L. A. Stern (1991). Mantle phase changes and deep-earthquake faulting in subducting lithosphere, *Science* **252,** no. 5003, 216–225.

Koper, K. D., M. E. Wysession, and D. A. Wiens (1999). Multimodal function optimization with a niching genetic algorithm: A seismological example, *Bull. Seismol. Soc. Am.* **89,** no. 4, 978–988.

LeFevre, L. V., and D. V. Helmberger (1989). Upper mantle *P* velocity structure of the Canadian Shield, *J. Geophys. Res.* **94,** no. B12, 17,749–17,765.

Li, G., L. Bai, Y. Zhou, X. Wang, and Q. Cui (2017). Velocity structure of the mantle transition zone beneath the southeastern margin of the Tibetan plateau, *Tectonophysics* **721,** 349–360.

Li, L., Y.-W. Chen, Y. Zheng, H. Hu, and J. Wu (2019). Seismic evidence for plume-slab interaction by high-resolution imaging of the 410-km discontinuity under Tonga, *Geophys. Res. Lett.* **46,** no. 23, 13,687–13,694.

Li, S.-H., Y.-B. Wang, Z.-B. Liang, S.-L. He, and Z. Wen-Hao (2012). Crustal structure in southeastern Gansu from regional seismic waveform inversion, *Chin. J. Geophys.* **55,** no. 2, 206–218.

Morgan, J. P., and P. M. Shearer (1993). Seismic constraints on mantle flow and topography of the 660-km discontinuity: Evidence for whole-mantle convection, *Nature* **365,** no. 6446, 506–511.

Mosegaard, K., and A. Tarantola (1995). Monte Carlo sampling of solutions to inverse problems, *J. Geophys. Res.* **100,** no. B7, 12,431–12,447.

Niazi, M., and D. L. Anderson (1965). Upper mantle structure of western North America from apparent velocities of *P* waves, *J. Geophys. Res.* **70,** no. 18, 4633–4640.

Niu, F., A. Levander, S. Ham, and M. Obayashi (2005). Mapping the subducting Pacific slab beneath Southwest Japan with Hi-net receiver functions, *Earth Planet. Sci. Lett.* **239,** nos. 1/2, 9–17.

Ringwood, A. E. (1975). *Composition and Petrology of the Earth's Mantle*, MacGraw-Hill, 618 pp.

Ritsema, J., W. Xu, L. Stixrude, and C. Lithgow-Bertelloni (2009). Estimates of the transition zone temperature in a mechanically mixed upper mantle, *Earth Planet. Sci. Lett.* **277,** nos. 1/2, 244–252.

Shearer, P. M. (2000). Upper mantle seismic discontinuities, *Geophys. Monogr. Ser.* **117,** 115–132.

Stoffa, P. L., and M. K. Sen (1991). Nonlinear multiparameter optimization using genetic algorithms: Inversion of plane-wave seismograms, *Geophysics* **56,** no. 11, 1794–1810.

Tajima, F., and S. P. Grand (1995). Evidence of high velocity anomalies in the transition zone associated with Southern Kurile subduction zone, *Geophys. Res. Lett.* **22,** no. 23, 3139–3142.

Tao, K., S. P. Grand, and F. Niu (2018). Seismic structure of the upper mantle beneath eastern Asia from full waveform seismic tomography, *Geochem. Geophys. Geosys.* **19,** no. 8, 2732–2763.

Tian, D., M. Lv, S. S. Wei, S. M. Dorfman, and P. M. Shearer (2020). Global variations of earth's 520- and 560-km discontinuities, *Earth Planet. Sci. Lett.* **552,** 116600.

Vidale, J. E., and H. M. Benz (1992). Upper-mantle seismic discontinuities and the thermal structure of subduction zones, *Nature* **356,** no. 6371, 678–683.

Wang, B., and F. Niu (2010). A broad 660 km discontinuity beneath northeast China revealed by dense regional seismic networks in China, *J. Geophys. Res.* **115,** no. B6, doi: 10.1029/2009JB006608.

Wang, R. (1999). A simple orthonormalization method for stable and efficient computation of green's functions, *Bull. Seismol. Soc. Am.* **89,** no. 3, 733–741.

Wang, X., J. Li, and Q.-F. Chen (2017). Topography of the 410 km and 660 km discontinuities beneath the Japan Sea and adjacent regions by analysis of multiple-*ScS* waves, *J. Geophys. Res.* **122,** no. 2, 1264–1283.

Wang, Y., L. Wen, and D. Weidner (2009). Array triplication data constraining seismic structure and composition in the mantle, *Surv. Geophys.* **30,** nos. 4/5, 355–376.

Zhang, R., Q. Wu, Y. Li, and B. Romanowicz (2012). Lateral variations in *SH* velocity structure of the transition zone beneath Korea and adjacent regions, *J. Geophys. Res.* **117,** no. B9, doi: 10.1029/2011JB008900.

Zhu, L., and L. A. Rivera (2002). A note on the dynamic and static displacements from a point source in multilayered media, *Geophys. J. Int.* **148,** no. 3, 619–627.

Manuscript received 28 December 2020
Published online 12 May 2021